Untethered, Dynamic Robotic Fabrics Enabled by Actively-Rigid Variable Stiffness Fibers

Trevor L. Buckner, Xiaonan Huang, and Rebecca Kramer-Bottiglio*

A robot that uses fabrics as its core body material can be lightweight, compact, and highly flexible. Ideally, the robot's actuation, sensing, and structural support are provided by fiber-based components, designed to integrate with the fabric's soft and conformable nature while preserving its fiber architecture. Typically, variable stiffness fibers are used for the structural elements, functioning as "bones" that can be turned on and off as needed. However, many variable stiffness fibers are passively-rigid, only allowing the fabric to become soft when powered, while some require bulky external air or power supplies, making them untenable for untethered robotics. In this work, an electrically-driven variable stiffness fiber is presented that performs a flat-to-curved geometry transition, providing a rigid load-bearing structure when powered but remaining flexible otherwise. Design principles for pairing the actively-rigid variable stiffness fiber with a materially compatible fiber-based actuator are presented, and the actuator performance in different configurations is characterized. The variable stiffness fiber can be arranged into sturdy legs, stable enough for a robotic fabric to lift and hold its own battery pack and onboard electronics. This capability is demonstrated with a first-of-its-kind fully-untethered locomoting robotic fabric using two different quadruped gaits.
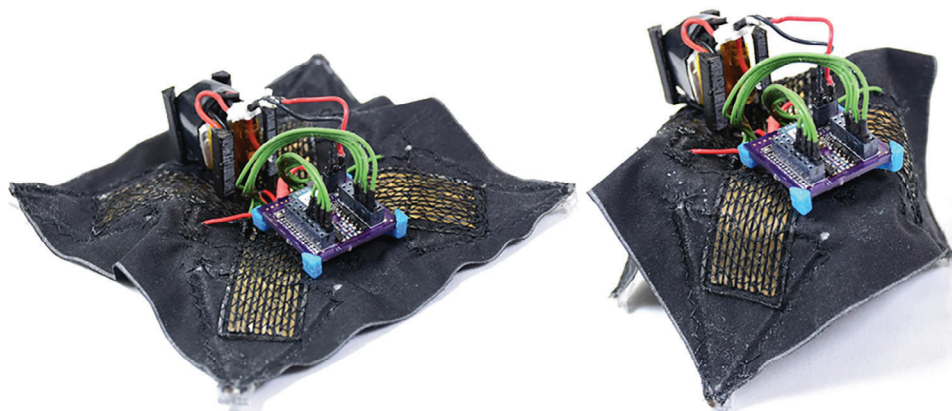
1. Introduction

Fabrics are not commonly associated with robots. However, consider a scenario in which an advanced piece of clothing autonomously folds itself in the laundry, a smart camping tent efficiently packs itself away, or an intelligent parachute adjusts its descent trajectory, and upon landing, crawls like an inchworm to its final designated location. While these examples may seem fanciful at first, pondering them suggests that, perhaps, robots need not be limited to the traditional steel-and-rivets vision that has occupied the public perception for so long. In fact, fabrics offer a unique and relatively underutilized design space for robotics. As a material, the interlaced fiber structure of fabrics carries a centuries-long reputation of being highly resilient,

flexible, lightweight, and adaptable to diverse applications. A wide variety of classic and technical fibers drives fabric usage as fireproof clothing, weather-protective barriers, and strong sails at sea. As a form factor, the flat, planar geometry of fabrics poses unusual challenges but also intriguing possibilities for robots that can be twisted, bent, and folded on the fly, changing shape to adapt to the task at hand, or simply for compact storage and later deployment.

Robots primarily made of fabric—or robotic fabrics—face an inherent challenge of overcoming the instability and nonlinear responses of a soft and flexible structure, which is exacerbated by the lack of a third dimension to be leveraged for geometric stability. A stabilizing structure is often provided by a variable stiffness mechanism, such that the robot can remain nominally soft but activate stiff regions when needed for load-bearing or to guide actuation paths. For robotic fabrics, these variable stiffness components are ideally implemented in a fiber-like form factor to retain the properties of the neat fiber architecture.[1] Components in a fiber format can be integrated smoothly into the base fabric substrate by weaving[2] or couching.[3,4] The change in stiffness can then be triggered via some stimulus, which could include an applied temperature change,[2,5] electrical current,[3,4,6] vacuum, or positive pressure,[7–16] mechanical tension,[17] or a variety of other means.[1,18]

Our prior work introduced an implementation of robotic fabrics with integrated functional fibers—actuation, sensing, and variable stiffness fibers—which enabled closed-loop control of common lightweight and breathable fabrics.[3] However, the prior robotic fabric suffered from key limitations that constrained the demonstrations to tethered and quasi-static (move-and-hold) motions. We attribute these limitations to our use of a passively-rigid variable stiffness fiber, which only becomes soft upon actuation (a common approach in the literature[2,4,5]). Our specific variable stiffness fiber selection in prior work[3] was also slow to switch between stiffness states (on the order of minutes), such that local stiffness tuning could not be used as part of a dynamic control policy. Finally, the prior variable stiffness fibers had no neutral configuration (i.e., the fibers would stiffen in whatever position they were cooled in), which meant that co-located actuators were required for variable stiffness fiber positioning.

T. L. Buckner, X. Huang, R. Kramer-Bottiglio
School of Engineering & Applied Science
Yale University
New Haven, CT USA
E-mail: rebecca.kramer@yale.edu

The ORCID identification number(s) for the author(s) of this article can be found under https://doi.org/10.1002/adfm.202404431

**ADVANCED
SCIENCE NEWS**

www.advancedsciencenews.com

**ADVANCED
FUNCTIONAL
MATERIALS**

www.afm-journal.de

Figure 1. Robotic Fabric. Passively-soft and actively-rigid beams allow this robotic fabric to support its own battery pack and onboard circuitry stably enough to stand up and walk. The fabric is a 120 mm square.

Because separate actuators were required for both positioning and behavior, our prior robotic fabric instantiation suffered from hardware and energy bulk that constrained the overall capabilities of the robot.

Herein, we present a robotic fabric implementation that uses an actively-rigid variable stiffness fiber, enabling passive system compliance and dynamic motions. The actively-rigid variable stiffness fiber is a patterned shape memory alloy (SMA; Nitinol) beam, which when heated naturally increases in stiffness as it undergoes a state transition from martensite to austenite, and further exhibits a flat-to-curved geometry transformation to yield a compound increase in the beam's stiffness. This variable stiffness SMA (VS-SMA) is also electrically-stimulated (i.e., boasts rapid stiffness switching) and self-straightening (i.e., does not require an antagonistic component to reverse deformation,[2–5] reducing part count), and so can be actuated with miniaturized onboard electronics and power, therefore lending to integration into untethered, dynamic robotic fabrics.

Below, we will cover the design and performance characterizations of VS-SMA, as well as include details of how VS-SMA can be used in conjunction with actuators and the necessary electronics to develop a thin, untethered, fabric-based locomotion robot (**Figure 1**).

2. Results

2.1. Design of VS-SMA

Our variable stiffness shape memory alloy (VS-SMA) beam is designed to achieve a significant change in stiffness after undergoing the shape-memory transition. At room temperature, the Nitinol we used is fairly flexible for a metal, (flexural modulus ≈66 GPa[3]). However, when heated above its Austenite Finish Temperature (A_f = 80 °C), Nitinol undergoes a state transition from martensite to austenite, causing an increase in modulus, up to 3× greater,[19] although this depends on processing and loading conditions.[20] On its own, this small increase in stiffness is not sufficient to act as a supportive beam, although it is a good start. To multiply this effect, we also program the VS-SMA to arch into a half-pipe when heated. This transition from a flat sheet at room temperature, to a 3D structure at elevated temperatures grants

the beam a geometrical stiffness advantage that can be tuned by adjusting the beam shape and programming parameters.
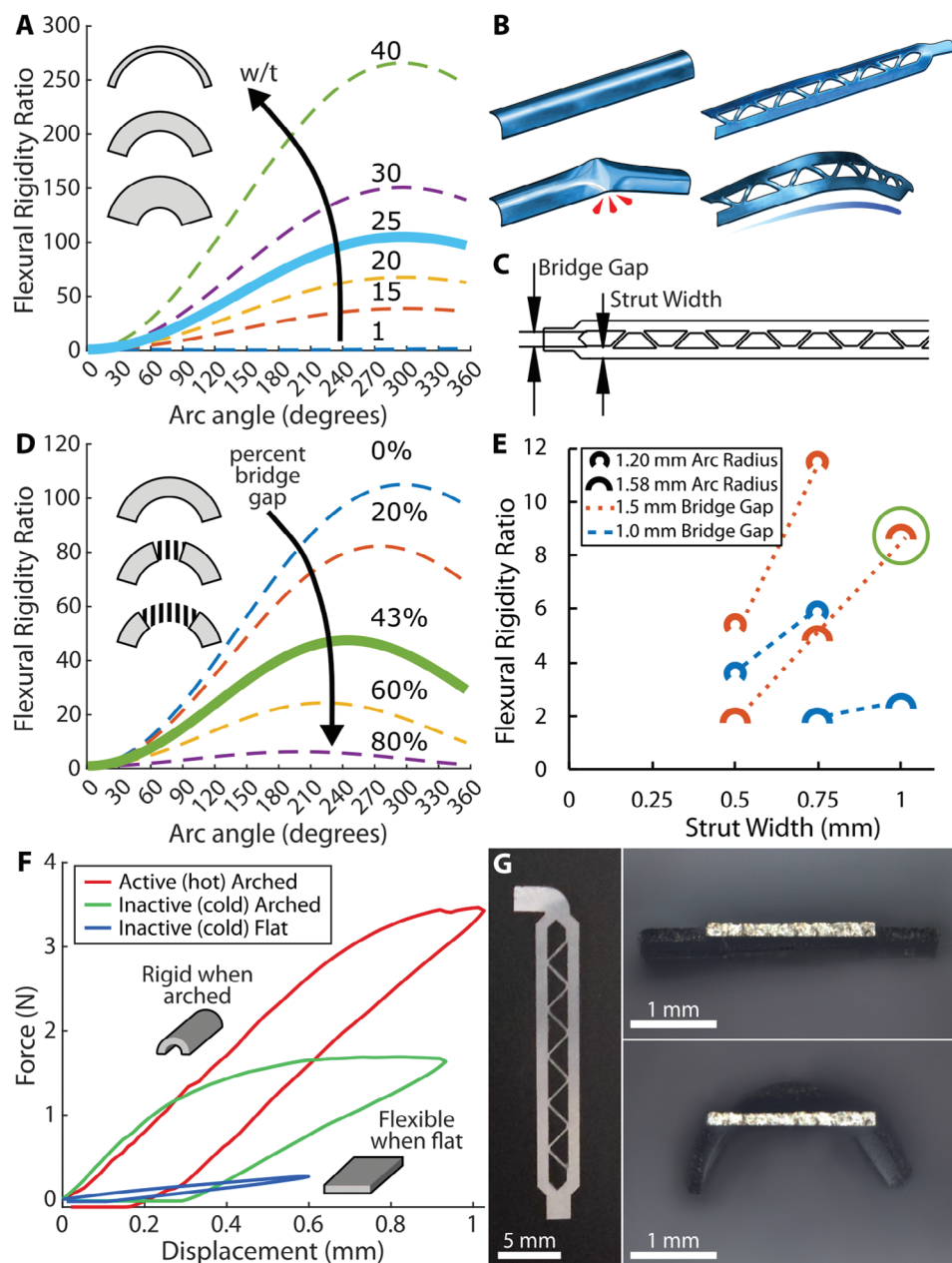
2.1.1. Mechanical Design

The tighter the radius of curvature of the arch, the higher the rigidity of the beam. This effect is increased for beams with a larger width-to-thickness (w/t) ratio, as the transition from flat to "3D" becomes more dramatic. Assuming the material modulus E is constant, the change in beam flexural rigidity EI_y can be described via an analytical model of the changing area moment of inertia I_y as the cross-section becomes curved into an arch (**Figure 2A**, Analytical Model for Arch Stiffness).

The arch design is constrained by a few parameters. To begin, we must consider size and space limitations. As discussed, a very wide and thin beam will provide the maximum stiffness change. However, a larger beam consumes more real estate in the robot and also requires increased current flow to reach target temperatures.

A second constraint is that the beam must be designed such that it can be returned to a flattened condition when stiffness is no longer desired and the heating stimulus has been removed. That is, attempting to bend the beam along its axis when cooled should collapse the beam back into a flat state. Unfortunately, the solid cross-section of the arch will instead cause the beam to pinch at localized sites rather than smoothly flatten, which causes stress damage at those regions (Figure 2B). To combat this, we removed material from the central portion of the arch, essentially dividing the cross-section into two parallel struts, attached at the edge with a sparse bridge (Figure 2C). The remaining material in the bridging pattern is still powerful enough to actuate the beam into an arched configuration and yet allows the beam to smoothly bend when heat is removed (Figure 2B) at the cost of a reduced variable stiffness range. The area moment of inertia I_y for the updated design was approximated analytically by treating the central bridge region of the arch as empty space (Analytical Model for Arch Stiffness). Figure 2D plots these values for the case where the w/t ratio is fixed at 25 (the thick line from Figure 2A).

A final constraint is that the maximum arch angle must be somewhat less than 180°. Otherwise, attempting to bend the

**ADVANCED
SCIENCE NEWS**

www.advancedsciencenews.com

**ADVANCED
FUNCTIONAL
MATERIALS**

www.afm-journal.de

Figure 2. VS-SMA Mechanical Design. A) Flexural rigidity of a beam with an arc cross-section, varying the arc angle and width-to-thickness ratio (normalized against a flat beam of the same dimension). The thick line marks our chosen aspect ratio. B) Solid beams will pinch and kink. Split beams bend smoothly with a gradual transition from arched to flat. C) Key shape parameters for the split-beam design: strut width and bridge gap. D) Flexural rigidity of a beam where the center portion of the arc has been removed (normalized against a flat beam with the same portion cut out). The thick line marks our chosen bridge gap. E) Various tested designs with differing strut widths, bridge gaps, and arc radii. Lines are used to group related designs. The circled point marks our chosen design. F) Representative force/displacement curves for a VS-SMA beam, demonstrating the difference in stiffness when flat and when heated to activate into an arch. The middle plot shows a beam that has been previously activated but has been allowed to cool, thus only a very short displacement is required to locally collapse back into a flat beam. G) The final chosen VS-SMA design, showing a top-down view and two profile views: flat and arched.

beam to flatten it may instead cause the arch to further compress into a circle.

Given these constraints, and following the predictions from our analytical model for maximizing the flexural modulus ratio, we experimentally tested a range of strut widths, bridge spacings, and arch curvatures (Figure 2E). Using a consistent material

thickness of 140 microns, each sample was laser-cut into the desired shape, inserted into a small brass tube to constrain it into an arched cross-section, and then heat-treated in an oven to set the arch into the Nitinol's shape memory. For each specimen, we used a three-point bending test to measure the flexural rigidity of the beam in its cold-flattened state, in its hot-arched state, and

ADVANCED
SCIENCE NEWS
www.advancedsciencenews.com

ADVANCED
FUNCTIONAL
MATERIALS
www.afm-journal.de

being bent back to flat after cooling down (Figure 2F). The maximum beam width was limited to 3.5 mm ($w/t = 25$) in consideration of the size constraint, and arch curvatures were limited by the tubing sizes available. Following experimentation, we also found that a bridge gap of at least 40% was needed to facilitate the return from arched to flat upon bending without pinching. In the end, we selected a design with parallel strut widths of 1 mm, and a bridge spacing of 1.5 mm, which provided a useful balance between size, stiffness change ratio ($\approx 8.8\times$), and ease of manufacture. Our radius of curvature was selected as 3.17 mm, giving an arc angle of approximately 126° (Figure 2G), safely below the 180° limit. We note that for these chosen parameters, Figure 2D predicts a flexural rigidity ratio of $\approx 25\times$; we attribute the difference to imperfections and nuances that the model does not account for. For instance, the bridged region of the beam is easier to bend than the struts, which causes a tighter localized curvature at the arc center. Additionally, deforming the VS-SMA away from its programmed configuration (flattening it), induces internal stresses that cause the flattened state to become more rigid than analysis of the geometry alone would predict.[21]

2.1.2. Electrical Design

Our VS-SMA beam was designed to be activated with Joule (resistive) heating, which allows it to be powered by a portable battery and easily managed via software. As long as the SMA is not physically damaged via plastic deformation, a target temperature of ≈ 100 °C allows for prolonged actuation, tested up to a fatigue life of >1000 cycles with no visible degradation in performance.[1,21] However, as with any resistive heating process, SMA is susceptible to cold regions that fail to activate, as well as hotspots and burnout, which anneals the material and reverts the programmed state. Hence, consistent heating is highly desired for reliable functioning of the VS-SMA component.

The VS-SMA bridging pattern has been structured such that current can flow as evenly as possible from terminal to terminal to reach a consistent temperature throughout the volume of the beam. Assuming a repeating 45° zig-zag bridge pattern, the beam can then be broken into sections and chained end-to-end to achieve beams of arbitrary length (**Figure 3A**), which can be automated using a parameterized CAD model (OnShape). Conceptually, the VS-SMA beam can be visualized as three parallel electrical pathways: the left strut, the right strut, and a narrow center zig-zag (Figure 3B). The two struts are of a constant width from end to end, and so on their own will heat evenly. However, introducing the center zig-zag complicates the electrical circuit, potentially diverting current unevenly between the two struts each time the zig-zag connects. This is solved however by noting that the zig-zag can be broken down further into the segments that run parallel to the strut walls, and the 45° cross beams that must traverse a longer length as they bridge the two struts (Figure 3C). If the extra traversal distance is accounted for by simply multiplying the width of the cross beam segments by a factor of $1/\cos(45°) = \sqrt{2}$, the electrical resistance per unit of axial length down the beam will remain constant for every segment along the entire zig-zag path. The net effect is that each of the two struts and the center zig-zag will have a constant current down the length of the beam, equivalent to three parallel resistors that only touch

at the ends. This can be verified by drawing the split segments in a simple circuit diagram. First, we reduce the number of variables by constraining resistances in the same pathway to be scalar multiples of each other (Figure 3C labels these scalars x and y.) Then, since we want each pathway to act as an independent resistor in parallel with the others, we add a further design constraint that the contact nodes between the three struts have a net zero current flow. The circuit can be evaluated under nodal voltage analysis to reveal the required resistance values of each segment (and hence, segment width) to achieve behavior that fits within these constraints. It turns out that any segment width will satisfy the equations generated by these constraints, as long as the scalar values x and y are equal. The resulting heating profile is visualized in a finite-element simulation (Solidworks 2021), confirming the lack of hot or severe cold spots in the struts (Figure 3D). The widening of the zig-zag cross beams does cause the bridge to receive a proportionally lower power density and hence it runs a little colder than the struts, although this is preferable to overheating. This behavior is also verified in physical specimens via a thermal camera (Fluke TiX 580) (Figure 3E).

Avoiding hotspots also requires a reliable electrical connection to any power source. Given the low electrical resistivity of Nitinol ($8.2 \times 10^{-6} \Omega$cm, about 4.8× that of copper), a beam of VS-SMA has a total resistance of <0.017 Ωcm^{-1}, which makes the system particularly sensitive to any small source of resistance and susceptible to hotspots and overheating. The wide and flat terminal shape resulting from the above electrical design also does not lend itself well to crimping, so instead components must be soldered. This solder bond also provides a sturdy mechanical link that resists loosening or displacement due to motion in the overall robotic system.

2.2. Design of Larger VS-SMA Support Structures

VS-SMA beams can be connected end-to-end in series via the same soldering approach mentioned above to achieve larger and more complex support structures (**Figure 4A**). For our robotic fabrics application, we have applied this concept to two main use cases.
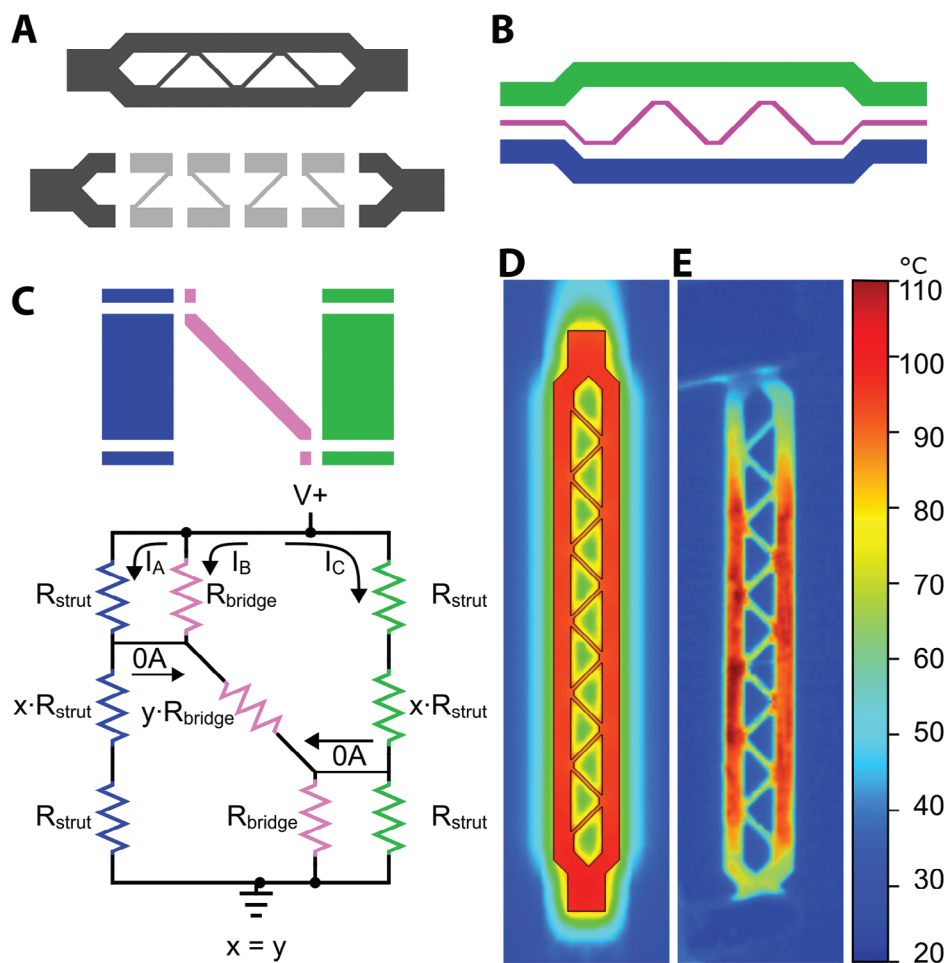
2.2.1. Load-Bearing Limbs

A variable stiffness system is often most directly used as a load-bearing mechanism. For example, we can arrange VS-SMA beams into a supportive "leg" with a triangular profile, and sew them onto a piece of fabric (Figure 4B). The two vertical beams are placed to share the load placed above, while the fabric tethers the beams together to prevent them from pulling apart (Figure 4C).

2.2.2. Rigid Frames for Force Application

When a chain of VS-SMA beams is used to circumscribe a section of fabric, it can act as a stabilizing frame. When activated, this VS-SMA frame will hold the contained fabric taut, causing the enclosed area to act as a rigid panel (Figure 4D). This rigid

ADVANCED
SCIENCE NEWS

www.advancedsciencenews.com

ADVANCED
FUNCTIONAL
MATERIALS

www.afm-journal.de

Figure 3. VS-SMA Electrical Design. A) The VS-SMA beam can be lengthened to an arbitrary size by adding additional segments, without complicating the electrical heating profile. B) The VS-SMA beam is designed as three parallel electrical pathways, two thick struts, and a center narrow zig-zag. C) A beam segment can be sliced further into smaller regions (top) to derive an equivalent circuit diagram (bottom). To aid in design calculations, some resistances are constrained to be multiples of others, scaled by variables x and y. Nodal analysis reveals that if the scalars x and y are equal, there will be a net zero current flow between the three pathways, equivalent to three independent currents in parallel. D) Joule-heating finite-element simulation shows the lack of hotspots. The bridge section is just slightly colder than the main struts. E) Thermal image of physical beam shows lack of hotspots. The ends are cold due to conduction into alligator clips.

panel provides a large stable interface against which actuators can be anchored to apply forces in a predictable direction. Several of these rigid panels can be placed in close proximity with edges parallel and separated by flexible hinges, similar to an origami structure. When each panel in a series is activated, the fabric is transformed from a flexible sheet to an articulated linkage (Figure 4E).
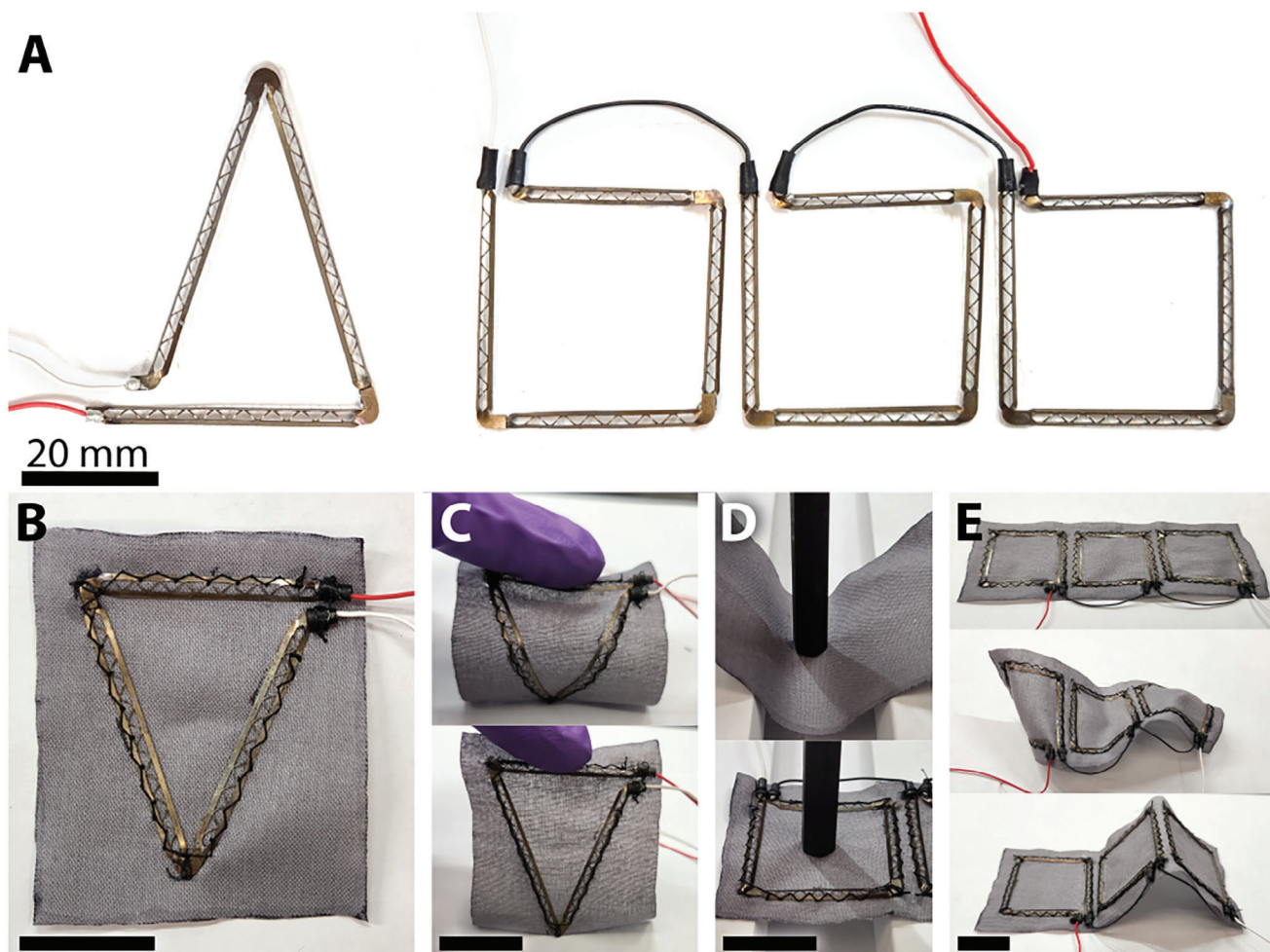
2.3. VS-SMA Integration with Bending Actuators

The novel design of VS-SMA was created for compatibility with bending actuators as a key feature. As demonstrated in our previous work,[3] Nitinol can also be used as an actuator for bending motion. In our prior work, we discussed a method for flattening off-the-shelf Nitinol wires into thin ribbons, which increased the reliability and actuating force when programmed to curl from a straight position. By placing those actuators back-to-back on a fabric, they can form an antagonistic actuating pair, which allows

for fully reversible, bidirectional motion. We also noted in Ref. [21] that stacking multiple thin ribbons can provide greater net forces compared to singular large ribbons, especially when paired against an opposing actuator whose stiffness must be overcome to generate motion.

2.3.1. Actuator Shape and Design

In this work, we decided to use the same ultra-thin ribbon design found in Ref. [21], but instead of stacking, the ribbons are arranged side-by-side in parallel to more evenly distribute them over the surface of the robot for more uniform overall flexibility of the fabric. The actuating ribbons are connected in electrical series in a serpentine pattern. A departure from earlier works, rather than form the actuators from flattened wire, we instead chose to laser-cut them from a Nitinol sheet as a contiguous trace. This added manufacturing precision eliminates many sources

ADVANCED
SCIENCE NEWS

www.advancedsciencenews.com

ADVANCED
FUNCTIONAL
MATERIALS

www.afm-journal.de

Figure 4. Larger VS-SMA Structures. All scale bars are 20 mm. A) VS-SMA beams can be soldered end-to-end to create larger shapes. B) VS-SMA beams sewn onto fabric. C) Supportive triangle easily flexes when inactive (top) but straightens and becomes rigid when active (bottom). D) Standard fabric draped over a gap collapses under a point load (top). An active VS-SMA frame pulls the whole region taut against pressure (bottom). E) A series of linked VS-SMA panels (top). When inactive, the panels easily flex and warp into an arbitrary shape (middle). When active, the panels straighten and become a rigid linkage (bottom).

of hotspots at junctures due to slight inconsistencies in cross-section, and also ensures even spacing between ribbons to avoid the chance of accidental shorting during use.
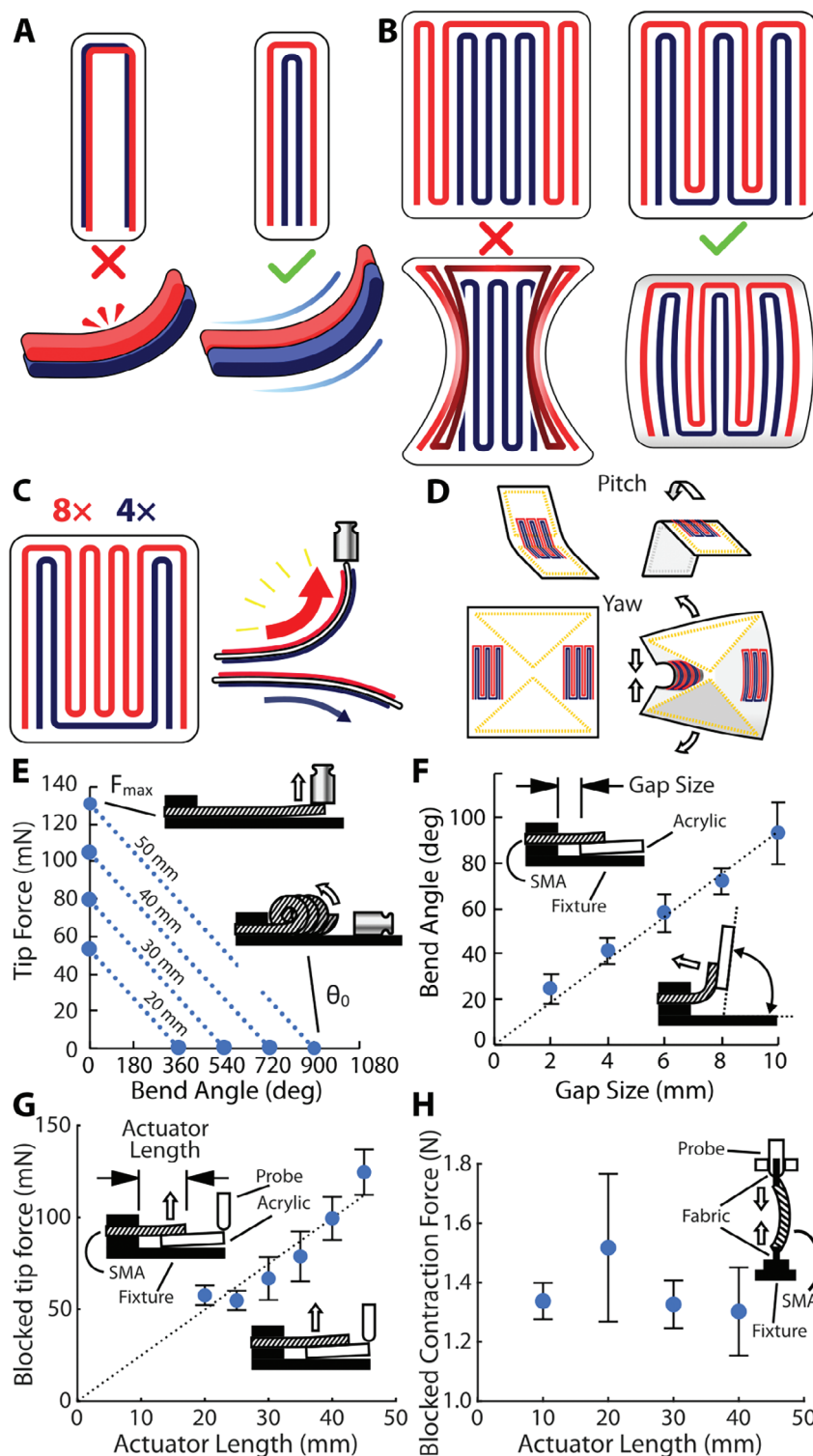
When pairing serpentine bending actuators in an antagonistic configuration, it is important that they not overlap, which would impose unnecessary resistance to motion, leading to losses in actuation force for both actuators by adding to the effective area moment of inertia. Instead, the serpentines should be interleaved in parallel so as to retain as thin a profile as possible (**Figure** 5A). Further, no one actuator should dominate either side or the outer region, else the actuation will become uneven with unintended motion as a result (Figure 5B). That is, the interleaved serpentines should be symmetrical, with the outer edges limited to one trace wide before changing actuators (Figure 5B). If one bending direction will require higher forces than the other, e.g., lifting a load against gravity versus lowering a load with help from gravity, the two actuator serpentines can be designed with differing numbers of total traces to reduce the antagonistic resistance in the high-force direction (Figure 5C), as long as the above rules

are also followed. Finally, antagonistic actuators can be placed on opposite faces of the fabric to mitigate thermal cross-talk. Note that even through the fabric, opposing actuators should still be interleaved to avoid overlapping.

2.3.2. Actuator Placement and Performance

Actuator size and placement in relation to VS-SMA frames will influence the total output force, as well as the maximum deflection achievable. Further, we show that it becomes possible to generate two separate motion types, pitch and yaw, (Figure 5D) while keeping all actuators within the plane of the fabric substrate.

The generation of force or displacement from a bending actuator can be characterized by its force-displacement curve, which differs depending on the actuator's length. Each curve is determined by two values, the nominal displacement θ_0 and the blocking tip force F_{max}. The nominal displacement is the maximum bending angle achieved when the actuator is operated freely from

**ADVANCED
SCIENCE NEWS**

www.advancedsciencenews.com

**ADVANCED
FUNCTIONAL
MATERIALS**

www.afm-journal.de

Figure 5. Actuator characterization. A) Antagonistic actuators stacked directly on top of each other will cause unnecessary stiffness in the system. Interleaving them side-by-side results in increased net actuation force. B) Interleaved antagonistic actuators should be symmetrical and distributed as evenly as possible to avoid unwanted force concentrations that result in undesirable motion. C) If one direction of motion requires higher forces, reducing the number of antagonistic traces will increase the net force in the primary bending direction by reducing the opposing stiffness to be overcome. D) Actuators (red and blue) and VS-SMA (yellow) can be arranged to generate both pitch and yaw motion. E) Force-displacement curve for sample bending actuators. F) For a fixed lever arm length, increasing the actuator length will proportionally increase the output bending tip force. G) For a fixed lever arm length, increasing the size of the flexible gap region will proportionally increase the output bending angle. H) When used for contraction, bending actuator length does not appear to affect the resulting blocked force.

a cantilevered fixture, without any external load. In the case of SMA bending actuators, this angle can be several hundred degrees as the actuator coils through several complete revolutions. The blocking tip force is the maximum force generated by the actuator. This force is achieved when the displacement of the actuator is completely blocked, that is, it works against a load with an infinitely high stiffness. In practice, however, the blocked force can be difficult to measure directly from a free-standing cantilever, as the actuator will tend to buckle rather than maintain zero displacement.

Instead, we can approximate the blocked force by following Euler-Bernoulli beam theory via $\theta = FL^2/2EI$, where I and L are the area moment of inertia and length of the actuator, and E is the flexural modulus of the actuator while active. However, rather than using F to deflect a straight cantilever, we begin with an active actuator that has already curled to achieve some tip angle θ, and F becomes the opposing tip force required to coerce the actuator back into its initial flat state. For $\theta = \theta_0$, $F = F_{max}$, and any value in between the unloaded and blocked states will follow a linear trend (Figure 5E). Thus, a desired intersection of force output and curvature can be achieved by adjusting the actuator length. Note that in practice, the actuator will always deliver some force value lower than F_{max}, since achieving the blocked force would require fully constraining the actuator from motion, such as by clamping the actuator flat against a table.

Bending Actuators (Pitch): By attaching a bending actuator across the fabric hinge between two adjacent VS-SMA frames, a fabric joint can be made to "pitch" up or down (Figure 5D, Movie S1, Supporting Information). Any portion of the actuator extending into one of the active and rigid VS-SMA frames will be unable to curl as it is held flat by the taut fabric. However, this does not prevent the constrained portion of the actuator from contributing to the bending force. On the other hand, only the portion of the actuator spanning the gap between VS-SMA frames will be able to bend, and thus the gap size will determine the maximum bending angle of this "hinge." A larger gap allows a longer portion of the ribbon to bend, while a narrow gap will result in very little curvature. We experimentally characterized the bending angle for different gap sizes by attaching bending actuators to pairs of acrylic tabs as stand-ins for the rigid VS-SMA frames. We applied a current (2.0 A) to the actuators and visually recorded the total angular deflection. Neglecting the weight of the acrylic tabs themselves, we see that indeed, the resulting bend angle appears to change approximately linearly with the gap size (Figure 5F).

We also measured the blocked bending force at the tip of the acrylic tab, while varying the length of the actuator extending into the rigid region. As expected, longer actuators result in a higher tip force, although they contribute little to the bending angle (Figure 5G). Of note, these results inform us that in an antagonistic actuator pairing, it is only necessary to overcome the bending stiffness for the portion of the opposing actuator in the hinge gap, as that is the only portion of the actuator that undergoes bending. That is, additional net actuation force can be achieved by extending further into the rigid VS-SMA frame region without also increasing the antagonistic stiffness. Note that by constraining the actuators against the table, we achieve blocked forces that closely match the approximated values in the force-displacement curve for any given actuator length (Figure 5E).

Bending Actuators (Yaw): When not in direct contact with a rigid VS-SMA frame, a bending actuator can still be used to impart a curvature to a surface or pull two points on the fabric toward each other. One interesting application of this is the ability to create a "yaw" joint within the plane of the fabric by using a bending actuator to pull two lever arms together. This motion can be pictured as the angle of a triangle becoming narrower as one edge contracts to pull the other two together (Figure 5D, Movie S2, Supporting Information). An actuator in this configuration acts as a linear contracting actuator, so we measured the blocked contraction force for varying actuator lengths (Figure 5H). In this case, we could not find a correlation between size and contraction force, although a longer actuator will of course have a larger total arc length, and hence can curl into a larger bend angle.

2.4. Application

Using VS-SMA as a viable thin, flexible, structural component and with accompanying compatible actuators, we designed a complete robotic structure to enhance a piece of plain woven cotton cloth such that it can stand and locomote under battery power. The robotic fabric is fully untethered and weighs 30.9 g.

2.4.1. Component Placement

Part of our aim with this design is that the base cloth should not require any additional cuts or holes to function properly. That is, the robot should rely on bending and folding rather than complex kirigami cutting patterns. This decision is mainly to demonstrate that even simple fabric pieces can be roboticized. To this end, we begin with a plain 12-cm square piece of woven cotton cloth. The four corners of the cloth will act as "legs" to stand and walk in a quadrupedal gait, and so are framed with VS-SMA to become triangular load-bearing limbs. The center of the robot body is also framed with VS-SMA to provide a stable central platform to hold the onboard electronics (Movie S3, Supporting Information).
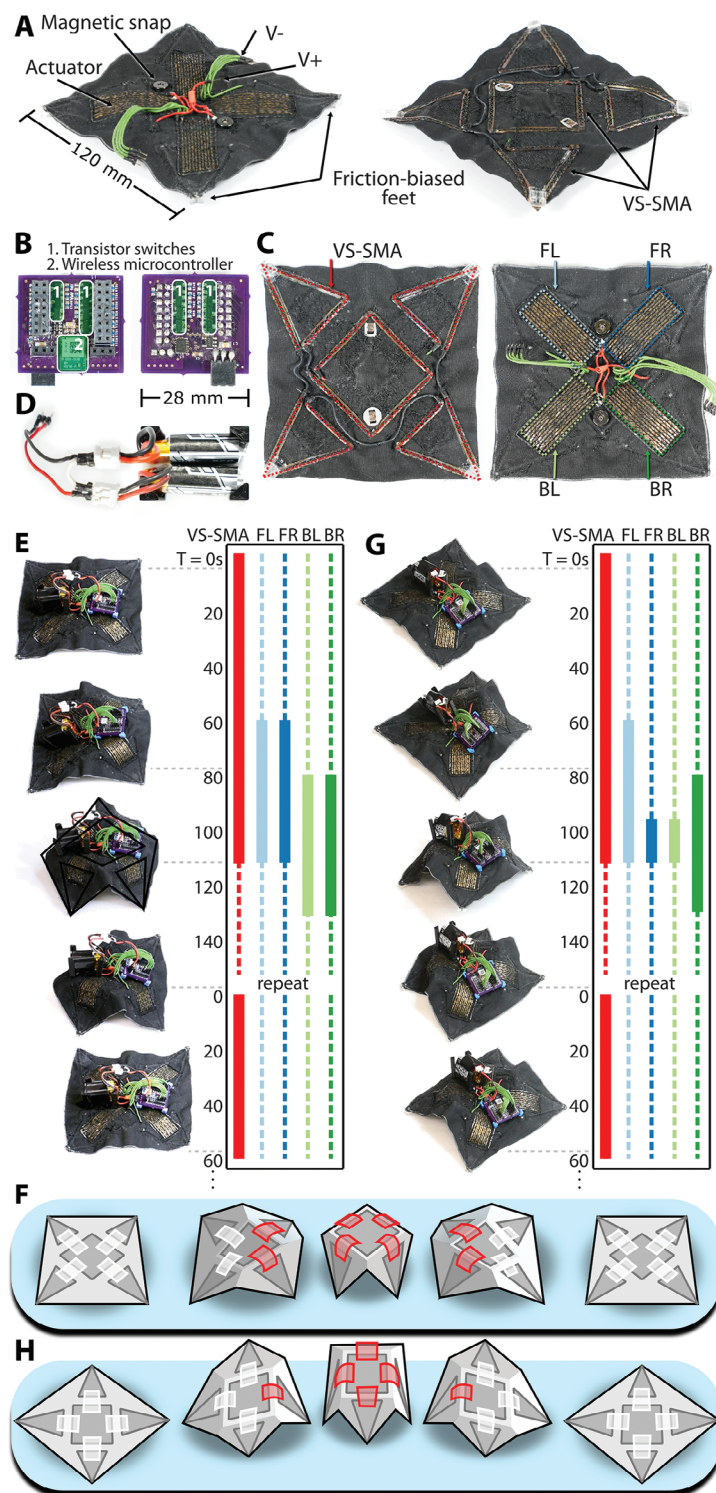
Bridging across the "knee joint" gaps between the central VS-SMA panel and each leg, we place "pitch" serpentine bending actuator. In this case, there is no need for an opposing antagonistic actuator, since the weight of the battery will provide the reversing force. Any overlapping SMA components are placed on opposing faces of the fabric, and any adjacent components are spaced at least 3.0 mm apart to reduce thermal cross-talk.[3]

Two magnetic fabric snaps are placed inside the central VS-SMA panel to act as an anchor for easy attachment and removal of the rigid electrical components (onboard PCB and battery). The rigid components are held in small 3D-printed (PLA) frames with corresponding magnetic snaps on the bottom. Four acrylic feet angled to provide anisotropic friction are attached with a silicone adhesive (Silpoxy, Smooth-on, Inc.) under the tips of all four triangle VS-SMA limbs (**Figure 6A**).

2.4.2. Controls

The robotic fabric can be teleoperated via Bluetooth from a laptop computer. The robot has an onboard BMD 350 module (U-Box)

ADVANCED
SCIENCE NEWS

www.advancedsciencenews.com

ADVANCED
FUNCTIONAL
MATERIALS

www.afm-journal.de

Figure 6. Robotic Fabric Design and Locomotion. A) The robotic fabric is a 120 mm square piece of fabric equipped with magnetic snaps for easy detachment of the onboard PCB and battery, a friction-biased foot at each corner, four bending leg actuators, a VS-SMA frame on the bottom, and the accompanying wiring to provide Joule heating current. B) The onboard PCB allows for teleoperation via Bluetooth and is capable of driving up to 15 separate SMA components at a time via an array of transistor switches. C) The SMA components include a single continuous VS-SMA chain, arranged into five rigid panels, and four legs: Front-Left (FL), Front-right (FR), Back-Left (BL), and Back-Right (BR). D) The battery pack can power the robot for approximately 20 min on a single charge. E) The first gait makes an inchworm-like motion by activating pairs of legs simultaneously. F) A drawing of the gait in (E). Active bending actuators are marked in red. G) The second gait makes another inchworm-like motion by activating diagonally opposed actuators, causing the robot to walk at an angle. The remaining two actuators are used only for stability. H) A drawing of the gait in (G). Active bending actuators are marked in red.

**ADVANCED
SCIENCE NEWS**

www.advancedsciencenews.com

**ADVANCED
FUNCTIONAL
MATERIALS**

www.afm-journal.de

that contains an nRF 52832 microcontroller and a Bluetooth antenna (Figure 6B). Bluetooth commands are sent from an nRF52 development kit that communicates with the laptop through UART. Each SMA component is labeled (VS-SMA, Front-Left, Front-Right, Back-Left, and Back-Right), and assigned to a different keyboard key on the laptop (Figure 6C). A pair of onboard 3.7V LiPo batteries (220 mAh, 5.9 g, 25 mm × 17 mm × 8 mm) connected in series are used to power the robot (Figure 6D). An external thermal camera (Fluke TiX 580) is used to monitor the temperature of all actuators to avoid overheating and overcooling.

Two inchworm-like gaits are implemented on the robotic fabric to achieve forward locomotion. Both gaits start with the activation of all VS-SMA panels so the fabric robot can hold its body weight, and they remain active while other SMA actuators are being actuated. For the first gait, we actuate the front two limbs to pull the fabric robot forward. Then, the rear two limbs are activated to bend inward to have frictional contact with the ground. Then, all SMAs and VS-SMAs are deactivated, which will cause the VS-SMA legs to collapse and buckle under the weight of the onboard PCB and batteries. The anisotropic frictional feet prevent the fabric robot from sliding backward during this collapse. Finally, the gait begins again by activating the VS-SMA, which straightens the legs and causes the robot to lunge forward slightly as it returns to its original flat configuration (Figure 6E,F, Movie S4, Supporting Information). The second gait starts with the actuation of one front leg to pull the robot toward the diagonal direction. The rear leg on the diagonal is actuated right after lifting the fabric robot up, which reduces friction and helps the robot pull forward. As the robot reaches its highest point, the two other legs are then actuated, lowering them to help keep balance. Similar to the first gait, all four legs and VS-SMA panels are then deactivated, causing the legs to buckle. In this case, beginning the next gait cycle does not seem to generate the same secondary lunge as the legs straighten out (Figure 6G,H, Movie S5, Supporting Information).

2.4.3. Locomotion Results

Both the forward crawling gait and the diagonal crawling gait enable the robotic fabric (total mass of 30.9 g, 12 cm × 12 cm) to crawl an average of ≈0.75 cm min^{-1}, or ≈0.07 body lengths per minute (BLPM) for 20 min, at which point the battery voltage has dropped low enough that powering multiple actuators simultaneously becomes difficult (825 J consumed, estimated by Coulomb counting from a limited number of trials). This leads to an approximate cost of transport (COT) of ≈18, 100. The robotic fabric translates ≈2.5 cm (0.22 body length) during the first gait cycle of both gaits. This is substantially larger than the remaining gait cycles since the robot starts from a fully flat shape at the beginning of the first cycle, while it cannot fully recover to the flat shape in the remaining gait cycles due to the absence of antagonistic actuators. However, it requires ≈50 s and ≈12 s, respectively, to fully actuate all VS-SMAs and one SMA during the first gait cycle due to the larger thermal barrier between the room temperature and the austenite finish temperature in the first cycle. The remaining gait cycles only require ≈70% of the actuation time compared with the first cycle since softening the VS-SMA during the de-

activation step only requires cooling below the martensite finish temperature, 40 °C.

3. Discussion

Designing a robot within the limitations of a fabric (extremely thin body, highly flexible, planar arrangement of components) comes with unusual challenges, but also poses an opportunity to push technologies toward new untested paradigms. The novel VS-SMA "actively-rigid" structural component represents one such advancement that may be used as a model for further technology developments, moving beyond the typically "passively-rigid" variable stiffness that is not appropriate for every use case. In addition to being "actively-rigid", VS-SMA is highly compatible with untethered systems, as it only requires electricity to function. Finally, VS-SMA automatically springs into its required shape, eliminating the need for a secondary actuator to move it into position. Each of these behaviors becomes especially valuable for robotic systems with very small profiles or that are otherwise designed for compactness.

The VS-SMA, and actively-rigid fibers in general, are preferable in many potential applications, as they allow a robotic fabric to remain flexible even when unpowered. For instance, several efforts have been made toward the development of smart textiles in wearable applications, the user should retain a free range of motion.[22–28] Similarly, a dynamic or locomoting robotic fabric benefits by retaining flexibility in its joints while only activating the "bones" it needs at a given time. Actively-rigid fabrics can also be folded or compressed for storage without first being activated for softening. Further, using actively-rigid variable stiffness fibers can drastically reduce the manufacturing complexity of a robotic fabric, as the fibers can be woven or threaded through a particular path in their passively soft state (as opposed to being softened and maintained in a soft state until placement of that component is complete).

Naturally, there is room for further improvement on this concept, and the design of VS-SMA comes with drawbacks of its own. Any thermally-driven mechanism like the VS-SMA tends to be susceptible to damage from overheating, and sensitive to environmental conditions. Thermally-driven systems are also extremely inefficient, as evidenced by our very high COT. A great deal of heat is constantly lost, requiring constant re-application of current to maintain the VS-SMA in an active state. Further, while it is possible to leverage controlled straightening and subsequent collapse of VS-SMA beams to generate motion, as demonstrated in the locomoting robot inchworm gaits, this process is also highly inefficient and slow. We also note that in pursuit of overcoming the obstacles described in the introduction, the total stiffness change ratio is somewhat low compared to other existing variable stiffness solutions.[1,29,30] However, our achieved value of 8.8× is on par with joint stiffening from human skeletal muscle[31] and is sufficient for functional robotic action. We believe that nascent material technologies may be able to overcome some of the above limitations, perhaps using the VS-SMA concept as a benchmark for future "actively-rigid" mechanisms.

The fiber-based nature of VS-SMA may also limit the total robot size. The scalability of fiber-based planar machines is influenced by factors such as the linear mass scaling of the robotic fabric unit and the power requirements for full activation, which

**ADVANCED
SCIENCE NEWS**

www.advancedsciencenews.com

**ADVANCED
FUNCTIONAL
MATERIALS**

www.afm-journal.de

also scale linearly with fiber length.[3] While driving forces from SMA bending actuators also scale linearly, support structures like VS-SMA fibers experience bending moments that scale quadratically with beam length, making long cantilevered regions less feasible.

The robotic fabric tightly integrates SMA actuators, VS-SMA, customized miniaturized electronics, and onboard power onto a piece of fabric, demonstrating fully untethered locomotion for the first time by a robotic fabric. This in and of itself is a notable feat, given the constraints of designing all components to be extremely thin. The seamless combination of VS-SMA and programmed SMA actuators provides both stiffness and force required for supporting the body weight and propelling the robot forward during actuation without sacrificing the flexibility of the fabric at room temperature.

For future work, we plan to integrate thermistors into the thermally-driven components of the robotic fabric, which can already be supported by our customized miniaturized PCB, capable of powering, controlling, and sensing the temperature of up to 15 SMA actuators. This may allow the robot to perform a locomotive gait autonomously while also monitoring temperatures to avoid burnout or damage. Further, we surmise that it may be possible to modify the VS-SMA design such that it mechanically locks and unlocks into the arched position, requiring power only to toggle between the soft and rigid states, thereby drastically increasing the speed and energy efficiency. With the demonstrated locomoting fabric as a base, computational tools can also be used to guide the design and control of future robotic fabric designs to generate more efficient gaits and perform more advanced tasks. In particular, we envision robotic fabrics that fold themselves into multiple configurations of the same body, perhaps walking as a quadruped over some difficult terrain, then curling into a tube for peristaltic motion through a small tunnel, before finally bending into a pincer to manipulate some object. Indeed, this work presents only a glimpse at the potential capabilities of robotic fabrics, with many improvements to come as fiber-based variable stiffness and actuation technologies develop.

4. Experimental Section

Analytical Model for Arch Stiffness: For a curved cross-section, the area moment of inertia $I_{y,\text{arch}}$ could be modeled as the area moment of inertia of a circular sector $I_{y,\text{sector}}$ of radius R with a smaller sector of radius r removed, where θ is the angle subtended by the arch:

$$
\begin{aligned}
I_{y,\text{sector}} &= \int_A \gamma^2 \, dA \\
&= \int_{-\frac{\theta}{2}}^{\frac{\theta}{2}} \int_0^r (r\cos\theta)^2 \cdot r \, dr \, d\theta \\
&= \int_{-\frac{\theta}{2}}^{\frac{\theta}{2}} \frac{r^4}{4} \cos^2\theta \, d\theta \\
&= \frac{r^4}{8}\left(\theta + 2\sin\frac{\theta}{2}\cos\frac{\theta}{2}\right)
\end{aligned}
\tag{1}
$$

$$
\begin{aligned}
I_{y,\text{arch}} &= I_{y,\text{sector},R} - I_{y,\text{sector},r} \\
&= \frac{R^4 - r^4}{8}\left(\theta + 2\sin\frac{\theta}{2}\cos\frac{\theta}{2}\right)
\end{aligned}
$$

The cross-section must then be shifted via the parallel axis theorem such that the beam is bent about the neutral axis $\bar{\gamma} = \sum A\gamma / \sum A$, where A is the area of the cross-section. The relevant components are found as follows:

$$
\begin{aligned}
\sum A_{\text{sector}} \gamma &= \int_A \gamma \, dA \\
&= \int_{-\frac{\theta}{2}}^{\frac{\theta}{2}} \int_0^r r\cos\theta \cdot r \, dr \, d\theta \\
&= \int_{-\frac{\theta}{2}}^{\frac{\theta}{2}} \frac{r^3}{3} \cos\theta \, d\theta \\
&= \frac{r^3}{3}\left(2\sin\frac{\theta}{2}\right)
\end{aligned}
\tag{2}
$$

$$
\begin{aligned}
\sum A_{\text{arch}} \gamma &= \sum A_{\text{sector},R} \, \gamma - \sum A_{\text{sector},r} \, \gamma \\
&= \frac{R^3 - r^3}{3}\left(2\sin\frac{\theta}{2}\right)
\end{aligned}
$$

$$
\begin{aligned}
\sum A_{\text{sector}} &= \int_A 1 \, dA \\
&= \int_{-\frac{\theta}{2}}^{\frac{\theta}{2}} \int_0^r r \, dr \, d\theta \\
&= \int_{-\frac{\theta}{2}}^{\frac{\theta}{2}} \frac{r^2}{2} \, d\theta \\
&= \frac{r^2}{2}\theta
\end{aligned}
\tag{3}
$$

$$
\begin{aligned}
\sum A_{\text{arch}} &= \sum A_{\text{sector},R} - \sum A_{\text{sector},r} \\
&= \frac{R^2 - r^2}{2}\theta
\end{aligned}
$$

Finally, these values can be fed into the parallel axis theorem $I_{y,\text{neutral}} = I_\gamma - A\bar{\gamma}^2$ to arrive at the shifted area moment of inertia for the arch:

$$
I_{y,\text{neutral,arch}} = I_{y,\text{arch}} - A_{\text{arch}}\left(\frac{\sum A_{\text{arch}}\gamma}{\sum A_{\text{arch}}}\right)^2
\tag{4}
$$

At this point, given a constant beam width w and beam thickness $t = R - r$, different arc angles could be iterated using $\theta = w / \left(R - \frac{t}{2}\right)$ and plot the change in area moment of inertia. Figure 2A demonstrates how the ratio of w/t affects the beam stiffness ratio increase normalized against a flat beam.

To account for the cutout bridge section, the analysis could be repeated as above, using a narrower angle $\phi = \theta \cdot \text{bridge\%}$. The resulting values can then be subtracted from those for a solid arch as follows:

$$
\bar{\gamma} = \frac{\sum A_{\text{arch,solid}}\gamma - \sum A_{\text{arch,bridge}}\gamma}{A_{\text{arch,solid}} - \sum A_{\text{arch,bridge}}}
$$

$$
\sum A_{\text{arch}} = \sum A_{\text{arch,solid}} - \sum A_{\text{arch,bridge}}
$$

$$
I_{y,\text{arch}} = I_{y,\text{arch,solid}} - I_{y,\text{arch,bridge}}
\tag{5}
$$

$$
I_{y,\text{neutral,arch}} = I_{y,\text{arch}} - A_{\text{arch}}\left(\frac{\sum A_{\text{arch}}\gamma}{\sum A_{\text{arch}}}\right)^2
$$

**ADVANCED
SCIENCE NEWS**

www.advancedsciencenews.com

**ADVANCED
FUNCTIONAL
MATERIALS**

www.afm-journal.de

VS-SMA Manufacture: The Nitinol alloy was purchased as a thin, 0.14 mm sheet (Baoji Seabird Metal Materials Co., Ltd.). This sheet was then laser-cut (LPKF ProtoLaser U4) into individual beams of the desired pattern, usually in a large batch (**Figure 7A**). The cut beams could then be removed from the sheet (Figure 7B), and the holes from the inner bridging pattern were punched out. Each beam was then manually bent along its cross-section with pliers to achieve an arch (Figure 7C). Each beam was then inserted into a cut brass tube of the desired inner radius to constrain the beam in an arch, leaving one of the electrodes protruding from the tube so that the beam could be easily pulled out later (Figure 7D). The sleeved beams were then placed in an oven (Thermo Scientific, Lindberg Blue M) at 390 °C for 20 min (Figure 7H), after which they were removed and quickly quenched in room-temperature water (Figure 7I). The tubes were then drained of any water and returned to the oven. This heating and quenching process was performed a total of three times. The beams could then be removed from their brass sleeves (Figure 7J) and flattened (Figure 7L). At this stage, individual beams of VS-SMA could be soldered together into a frame structure, or attached to flexible silicone wire leads for power.

VS-SMA Flexural Stiffness Measurement: The flexural moduli of the various VS-SMA beam designs in Figure 2E were measured using a dynamic mechanical analyzer (DMA Q800; TA Instruments). Specimens were sized to a length of 50 mm and placed onto a three-point bending fixture with a support separation of 15 mm. All specimens were held at a constant temperature (23 °C or 100 °C) and then subjected to a strain ramp of 4 mm/min to a maximum deflection of 2 mm. Each specimen was tested in three different scenarios: Flattened at room temperature, arched at 100 °C, and arched at room temperature (collapsed back to flat).

Bending Actuator Manufacture: Similar to the VS-SMA manufacturing steps, the bending actuators were laser-cut (LPKF ProtoLaser U4) from a sheet of 0.14 mm Nitinol (Baoji Seabird Metal Materials Co., Ltd.), including a surrounding rectangular frame to give the thin serpentine pattern some stability during processing (Figure 7A). The Nitinol rectangle was taped over on both sides using cellophane tape to further prevent the serpentine cutout from coming loose and tangled (Figure 7E). The entire rectangle was then coiled tightly into a cylinder using high-gauge round-nose pliers (Figure 7F). This cylinder was then inserted into a brass tube of 6.35 mm (1/4 inch) inner diameter to constrain the serpentine in a coil (Figure 7G). The tube was then placed in an oven (Thermo Scientific, Lindberg Blue M) at 390 °C for 20 min (Figure 7H), after which they were removed and quickly quenched in room-temperature water (Figure 7I). The tube was then drained of any water and returned to the oven. This heating and quenching process was performed a total of three times. The wrapped serpentine SMA could then be removed from its brass sleeve (Figure 7J). At this point, most of the cellophane tape would be melted away, and the Nitinol rectangle could be uncurled and separated from the serpentine actuator (Figure 7K). The actuator ends were soldered to flexible silicone wire leads for power (Figure 7M).

Actuator Force-Displacement Curve Approximation: Determining the actuator force-displacement curve required two values: the nominal displacement θ_0 and the blocked tip force F_{max}. Each specimen was made of a 0.14 × 1.0 mm bending actuator cut into a long, 10 mm-wide U-shaped path. The open end of the "U" was clamped to the table such that the remainder of the actuator length (20, 30, 40, or 50 mm) remains free to curl upward when activated. Specimens were activated with 2.0 A under zero load. θ_0 was then measured from the diameter D of the resulting coil via $\theta_0 = \pi D$.

F_{max} is determined by first measuring the actuator flexural modulus E. A materials tester (Instron 3345) was used to perform a three-point bending test on each specimen with a support span of 3 mm, and a loading rate of 0.1 mm/s, bending each specimen (six total specimens, measured once each) opposite its normal actuation direction. During the text, specimens were activated with 2.0 A such that the modulus measured was that of the activated austenite phase. The resulting E measured was 18.7 GPa, STD 4.1. Then, F_{max} can be approximated by following Euler-Bernoulli beam theory via $\theta = FL^2/2EI$, where I and L are the area moment of inertia and length of the actuator, as detailed previously in the text.

"Pitch" Actuator Blocked Bending Force Measurement: To characterize the effect of SMA length on actuation force, the blocked bending tip forces of several simple actuators were measured using a materials tester (Instron 3345). Each specimen was made of a 0.14 × 1.0 mm bending actuator cut into a long, 10 mm-wide U-shaped path. The open end of the "U" was clamped to the table such that the remainder of the actuator length (20, 25, 30, 35, 40, or 45 mm) remained free to curl upward when activated. After the first 10 mm of this free length, a 15 mm × 40 mm × 1.5 mm acrylic tab was super glued onto the remaining length. The acrylic tab constrains the affixed portion of the actuator from bending. In addition to the 40 mm tab, the 10 mm of unconstrained actuator makes up a 50 mm moment arm. The distal tip of the acrylic tab was positioned beneath the Instron probe such that the actuator was constrained flat against the table. Specimens were activated with 2.0 A, causing the actuators to press the acrylic tip upward against the probe to measure a blocked force until a steady state was reached. Each data point was the mean value of three specimens, measured once each. Despite being constrained from bending by the acrylic, longer actuators continue to generate higher forces for a given moment arm length.

"Yaw" Actuator Blocked Contraction Force Measurement: To characterize the effect of SMA length on linear contraction force, the blocked contraction forces of several simple actuators were measured using a materials tester (Instron 3345). Each specimen was made of a 0.14 × 1.0 mm bending actuator cut into a long, 10 mm-wide U-shaped path, sewn onto a cotton fabric strip. Actuators were sized to 10, 20, 30, or 40 mm long. The specimens were held vertically using a gripper fixture, clamped onto the exposed fabric at each end and flush against the top and bottom of the SMA. Specimens were activated with 2.0 A, causing the actuators to pull downward on the probe as they attempted to curl, measuring a blocked contraction force until a steady state was reached. Each data point was the mean value of three specimens, measured once each. In this case, there appeared to be no discernible relation between actuator length and output force.
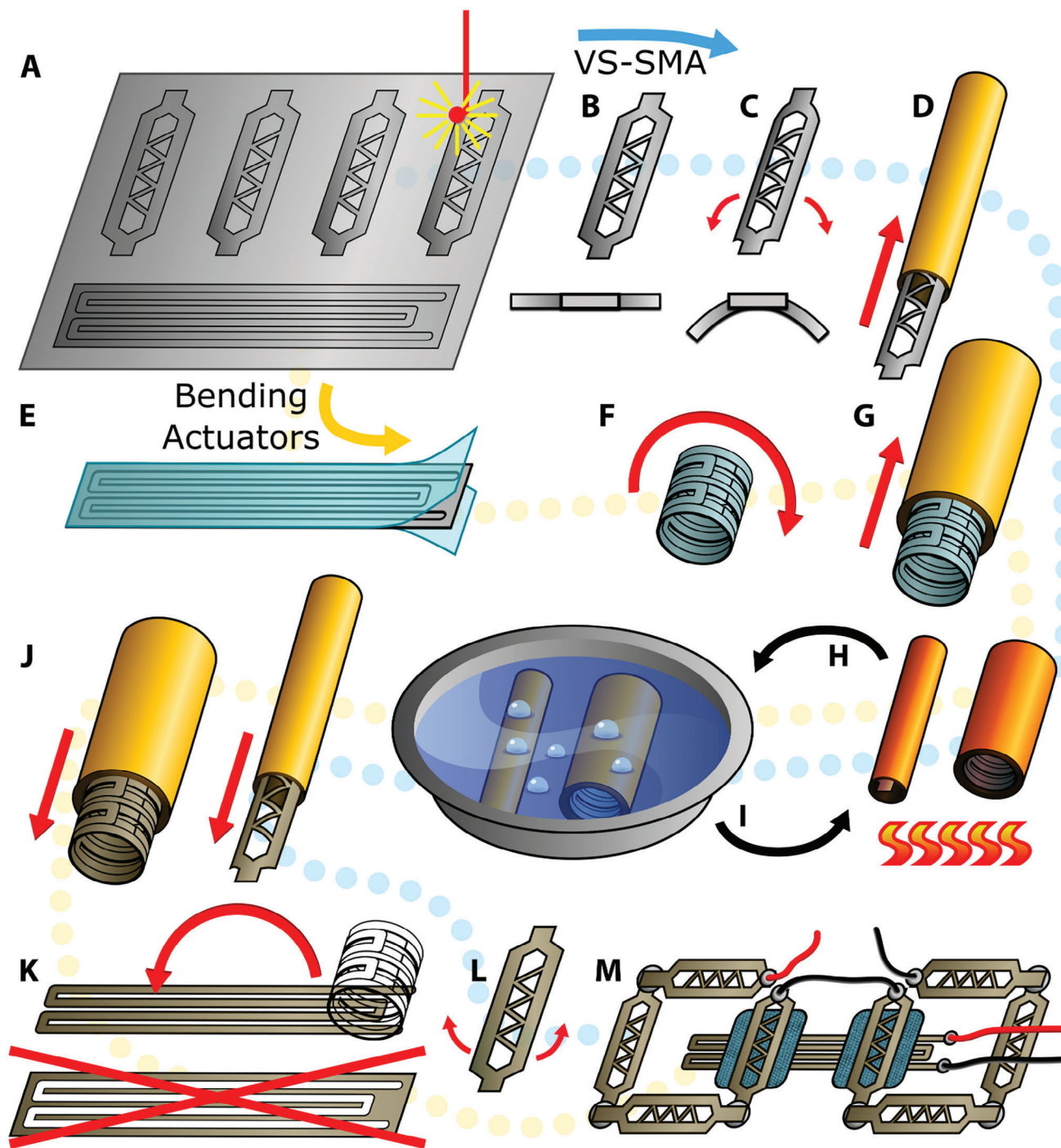
Nitinol Soldering: Nitinol tends to form titanium oxide on the metal surface rather quickly in the presence of air. However, assembly in a vacuum or an inert environment was not always feasible. Instead, it was possible to achieve a solder connection using aggressive flux (LA-CO, N3 All-Purpose Flux) to etch away the oxide, and using silver solder (96.5 Sn/3.5 Ag, SRA Soldering Products) which had become the standard for Nitinol soldering. The rapid formation of oxide also inhibits the usual expected wicking flow behavior of the solder. In order to attach two Nitinol segments together, each segment was individually etched with flux and tinned with a small bead of solder, after which the two ends could be pressed together and heated, allowing the two solder beads to reflow and join.

Robot Assembly: The locomoting robotic fabric was assembled by hand. First, the cotton fabric was cut to the desired shape, and the edges were given a light coating of a liquid fray check sealant (Dritz Fray Check). Locations for each component were carefully marked with a felt marker through a paper stencil. The prepared VS-SMA beams and bending actuators were then couched directly onto the fabric using a sewing machine, making sure to follow the full trace of any serpentine patterns to ensure the entirety of the actuator was firmly attached to the fabric. The sewing step must be taken slowly to avoid accidentally punching into and buckling any SMA components. At this stage, all power leads could be routed toward the eventual PCB anchor point, cutting small holes in the fabric to pass wires through if needed. The V+ lines were soldered together, while the V- lines were attached to a set of header pins to ease connection to the PCB later. Any long loose wires could be sewn down.

With the core structure of the robot in place, the biased acrylic feet could be manufactured. These were laser-cut into flat panels with a protruding hook. The hook was then filed down to a point to create a pointed tooth, which grips in the hook direction, but could slide easily in the opposite direction or to either side. One foot was attached at the tip of each fabric corner using silicone adhesive (Silpoxy, Smooth-on, Inc.), and the teeth were aligned with the bending actuators.

Finally, magnetic snaps were punched into the desired anchor points for the battery and onboard PCB, for easy detachment.

ADVANCED
SCIENCE NEWS

www.advancedsciencenews.com

ADVANCED
FUNCTIONAL
MATERIALS

www.afm-journal.de

Figure 7. VS-SMA and Bending Actuator Manufacture. A) SMA components are laser-cut from a sheet of Nitinol. B) VS-SMA beams are separated from the sheet. C) VS-SMA beams are bent into an arc. D) VS-SMA beams are inserted into a brass tube to maintain the arch during heat treatment. E) Bending actuators are also removed, and covered in tape to keep thin traces in position. F) Bending actuators are coiled into a cylinder. G) Bending actuators are inserted into a brass tube to maintain the coil during heat treatment. H) SMA components are heated in an oven 390 °C. I) SMA components are quenched in water and then returned to the oven. J) SMA components are removed from brass tubes. K) Bending actuators are flattened and separated from the remaining material. L) VS-SMA beams are flattened. M) SMA components can be soldered together in a frame and attached to flexible silicone wire for power.

Onboard Electronics: The PCB was designed to be small (28 mm × 26 mm) and lightweight (5.8 g), yet must also be able to route high current (≈5 A) from the battery to each SMA component. The customized PCB was composed of a BMD 350 module that contains an nRF 52832 microcontroller and a Bluetooth antenna, 15 N-MOSFETs (AO3416) that were used as switches to control up to 15 SMA actuators, a voltage regulator (AP2210K) to pull down the voltage from 7.4 to 3.3 V to power the microcontroller, and a multiplexer (74HC4051) that could select analog input signal for closed-loop control of the robotic fabric in a future iteration. A pair of small and light 3.7V LiPo batteries (25 mm × 17 mm × 8 mm, 5.9 g, 220 mAh) were connected in series to power the robot.

Supporting Information

Supporting Information is available from the Wiley Online Library or from the author.

Conflict of Interest

The authors declare no conflict of interest.

Data Availability Statement

The data that support the findings of this study are available from the corresponding author upon reasonable request.

[1] T. L. Buckner, R. Kramer-Bottiglio, *Multifunct. Mater.* **2018**, *1*, 012001.
[2] A. Tonazzini, S. Mintchev, B. Schubert, B. Mazzolai, J. Shintake, D. Floreano, *Adv. Mater.* **2016**, *28*, 10142.
[3] T. L. Buckner, R. A. Bilodeau, S. Y. Kim, R. Kramer-Bottiglio, *Proc. Natl. Acad. Sci.* **2020**, *117*, 25360.
[4] M. C. Yuen, R. A. Bilodeau, R. K. Kramer, *IEEE Robot. Autom. Lett.* **2016**, *1*, 708.
[5] H. M. Le, L. Cao, T. N. Do, S. J. Phee, *Mechatronics* **2018**, *53*, 109.
[6] J. Piao, M. Kim, J. Kim, C. Kim, S. Han, I. Back, J.-s. Koh, S. Koo, *Sci. Rep.* **2023**, *13*, 4869.
[7] X. Liang, H. Cheong, Y. Sun, J. Guo, C. K. Chui, C.-H. Yeow, *IEEE Robot. Autom. Lett.* **2018**, *3*, 2702.
[8] M. Brancadoro, M. Manti, S. Tognarelli, M. Cianchetti, *Soft Robot.* **2020**, *7*, 663.
[9] S. Jadhav, M. R. A. Majit, B. Shih, J. P. Schulze, M. T. Tolley, *Soft Robotics* **2022**, *9*, 173.
[10] I. Andrade-Silva, J. Marthelot, *Adv. Intell. Syst.* **2023**, *5*, 2200435.
[11] Z. Zhang, Y. Long, G. Chen, Q. Wu, H. Wang, H. Jiang, *Sci. Adv.* **2023**, *9*, eadg1203.
[12] D. Quevedo-Moreno, E. T. Roche, *IEEE Robot. Autom. Lett.* **2023**, *8*, 3110.
[13] A. Bhat, S. S. Jaipurkar, L. T. Low, R. C.-H. Yeow, *Soft Robotics* **2023**, *10*, 923.
[14] V. Sanchez, K. Mahadevan, G. Ohlson, M. A. Graule, M. C. Yuen, C. B. Teeple, J. C. Weaver, J. McCann, K. Bertoldi, R. J. Wood, *Adv. Funct. Mater.* **2023**, *33*, 2212541.
[15] Y. Zhao, Y. Wang, *IEEE Robot. Autom. Lett.* **2023**, *8*, 3238.
[16] J. Xu, Y. Zhang, Y. Huang, L. Chang, T. Chen, T. Ren, Z. Cai, *Int. J. Mech. Sci.* **2024**, *264*, 108840.
[17] T. M. Huh, Y.-J. Park, K.-J. Cho, *Int. J. Precis. Eng. Manuf.* **2012**, *13*, 1255.
[18] L. Blanc, A. Delchambre, P. Lambert, *Actuators* **2017**, *6*, 23.
[19] K. Otsuka, C. M. Wayman, *Shape Memory Materials*, Cambridge University Press, Cambridge **1999**.
[20] A. N. Bucsek, H. M. Paranjape, A. P. Stebner, *Shape Mem. Superelasticity* **2016**, *2*, 264.
[21] T. L. Buckner, R. Kramer-Bottiglio, in *2021 IEEE 4th International Conference on Soft Robotics (RoboSoft)*, IEEE, Piscataway, NJ **2021**, pp. 579–582.
[22] E. T. Roche, M. A. Horvath, I. Wamala, A. Alazmani, S.-E. Song, W. Whyte, Z. Machaidze, C. J. Payne, J. C. Weaver, G. Fishbein, J. Kuebler, N. V. Vasilyev, D. J. Mooney, F. A. Pigula, C. J. Walsh, *Sci. Transl. Med.* **2017**, *9*, eaaf3925.
[23] T. H. Koh, N. Cheng, H. K. Yap, C.-H. Yeow, *Front. Neurosci.* **2017**, *11*, 597.
[24] L. Rosalia, C. Ozturk, J. Coll-Font, Y. Fan, Y. Nagata, M. Singh, D. Goswami, A. Mauskapf, S. Chen, R. A. Eder, E. M. Goffer, J. H. Kim, S. Yurista, B. P. Bonner, A. N. Foster, R. A. Levine, E. R. Edelman, M. Panagia, J. L. Guerrero, E. T. Roche, C. T. Nguyen, *Nat. Biomed. Eng.* **2022**, *6*, 1134.
[25] B. W. Ang, C.-H. Yeow, in *2019 2nd IEEE International Conference on Soft Robotics (RoboSoft)*, IEEE, Piscataway, NJ **2019**, pp. 577–582.
[26] R. Granberry, J. Abel, B. Holschuh, in *Proceedings of the 2017 ACM International Symposium on Wearable Computers - ISWC '17*, ISWC '17. ACM Press, Maui, Hawaii, **2017**, pp. 186–191.
[27] J. W. Booth, D. Shah, J. C. Case, E. L. White, M. C. Yuen, O. Cyr-Choiniere, R. Kramer-Bottiglio, *Sci. Rob.* **2018**, *3*, 22.
[28] V. Sanchez, C. J. Walsh, R. J. Wood, *Adv. Funct. Mater.* **2021**, *31*, 2008278.
[29] M. Manti, V. Cacucciolo, M. Cianchetti, *IEEE Robot. Autom. Mag.* **2016**, *23*, 93.
[30] T. L. Buckner, M. C. Yuen, S. Y. Kim, R. Kramer–Bottiglio, *Adv. Funct. Mater.* **2019**, *0*, 1903368.
[31] J. D. W. Madden, N. A. Vandesteeg, P. A. Anquetil, P. G. A. Madden, A. Takshi, R. Z. Pytel, S. R. Lafontaine, P. A. Wieringa, I. W. Hunter, *IEEE J. Oceanic Eng.* **2004**, *29*, 706.